

# Chapter 4: Defects and Doping Engineered 2D o-B<sub>2</sub>N<sub>2</sub> for HER Activity

---

## 4.1 Introduction

Global population growth drives increased energy demands.<sup>1</sup> Non-renewable fossil fuels like petrol, diesel and oil are depleting and polluting, necessitating cleaner alternatives. Hydrogen is a promising renewable energy option, produced through water splitting using either photocatalysts or electrocatalysts. Efficient catalysts are needed for the HER activity.<sup>2</sup> Challenges include slow kinetics and high overpotential. Pt and its alloys are effective but costly and scarce.<sup>3</sup> Scientists seek cheaper, abundant catalysts for sustainable hydrogen energy.

Due to the exceptional properties of 2D materials, they have attracted significant attention in the catalyst field after the discovery of graphene.<sup>4-6</sup> Two key advantages of 2D materials as catalysts for HER activity are their large surface to volume ratio, which provides numerous sites for reaction; and their easily adjustable structural and electrical properties through doping of foreign atoms or defect condition.<sup>7,8</sup> Graphene and g-C<sub>3</sub>N<sub>4</sub> are unsuitable for HER activity due to their positive and excessively negative  $\Delta E_{\text{ads}}^{\text{H}}$  values, respectively. The positive  $\Delta E_{\text{ads}}^{\text{H}}$  of graphene (0.8 eV) hinders H atoms from adsorbing on its surface, while the excessively negative adsorption energy of g-C<sub>3</sub>N<sub>4</sub> (-0.50 eV) makes the desorption process challenging during HER activity.<sup>9,10</sup> Sathe et al. conducted the study to improve the HER activity of the graphene and found that the enhancement in the HER activity of the graphene after B doping.<sup>11</sup> Similarly, S doped graphene with plasma-etching has also been reported to exhibit excellent HER activity, with an overpotential of 178 mV.<sup>12</sup> In the same direction, Lim et al. studied the HER activity of Fe doped into vacancy defected graphene and found a highly

commendable results.<sup>13</sup> Furthermore, the introduction of dopants such as S, Na and O has been found to enhance the catalytic activity for HER in the case of g-C<sub>3</sub>N<sub>4</sub> in comparison to its pure g-C<sub>3</sub>N<sub>4</sub>.<sup>14-16</sup> One of the allotropes of the graphene i.e. penta-graphene has also been explored for the HER catalyst under pristine, defect and doping condition and found significant improvement.<sup>17</sup> Another 2D material similar to graphene is h-BN with insulating properties having band gap of about 5.8 eV.<sup>18</sup> However, its insulating behavior limits its use as a photocatalyst.<sup>18</sup> The studies suggest that introducing vacancies and doping can alter structural, electronic and chemical properties of h-BN.<sup>19-21</sup> The theoretical study by Sredojević et al. reported the HER activity of transition metals doped defected graphene and h-BN and found that the HER activity of these materials reached the values comparable to the ideal case.<sup>19</sup> In addition, the incorporation of C atoms into the h-BN structure enhances its catalytic properties, making it well-suited for facilitating the activation and reduction of oxygen molecules.<sup>20</sup> According to Wan et al., p-BN shares similarities with h-BN in terms of being a wide band gap semiconductor with an insulating nature, which initially renders it unsuitability for catalytic reaction. In addition, through the introduction of C doping, the band gap of p-BN can be tuned. This modification allows p-BN to become an effective metal-free photocatalyst capable of facilitating complete water splitting.<sup>21</sup> The above literature survey indicates that the creation of defects and doping is one of the most effective techniques for enhancing the HER activity of various 2D materials.

Demirci et al. recently discovered a stable orthorhombic diboron dinitride (o-B<sub>2</sub>N<sub>2</sub>) monolayer, exhibiting semiconductor properties with 0.64 eV band gap. This unique material possesses anisotropic electronic and mechanical characteristics, similar to h-BN, due to its diatomic building blocks. Potential synthesis can be achieved using precursor materials containing N-N and B-B bonds.<sup>22</sup> Furthermore, DFT investigation by Kumawat et al. revealed that the 2D o-B<sub>2</sub>N<sub>2</sub>, unlike h-BN, exhibits strong directional anisotropic behavior in transport

properties, such as electric current and electronic transmission function. This characteristic makes 2D o-B<sub>2</sub>N<sub>2</sub> a promising candidate for directional-dependent applications in nanoscale devices like optoelectronics, magneto-transport and anisotropic electric transport.<sup>23</sup> Khossossi et al. demonstrated the application of 2D o-B<sub>2</sub>N<sub>2</sub> as electrode material for rechargeable Li- and Na-ions batteries, employing DFT simulations.<sup>24</sup> Additionally, a research study has proposed Li decorated o-B<sub>2</sub>N<sub>2</sub> as a hydrogen storage medium. The findings of this study reveal that this material exhibits a remarkable capacity for storing hydrogen, amounting to 12.4 wt%.<sup>25</sup> The Kadhim et al. and their collaborators investigated the sensing properties of the 2D o-B<sub>2</sub>N<sub>2</sub> towards acetone gas and propylene oxide. The study predicted that the 2D o-B<sub>2</sub>N<sub>2</sub> exhibits favourable sensing properties for both molecules, indicating its potential as a remarkable sensing material.<sup>26,27</sup>

Based on our comprehensive literature survey, the potential catalytic application of 2D o-B<sub>2</sub>N<sub>2</sub> in the HER activity remains unexplored. In this study, we investigated the HER activity of pristine 2D o-B<sub>2</sub>N<sub>2</sub> with vacancy defects and C doping using DFT simulations. For practical consideration, we have also evaluated room temperature stability using AIMD calculation of defected and C doped 2D o-B<sub>2</sub>N<sub>2</sub>.

## 4.2 Computational Details

All necessary computations were carried out utilizing first-principles based DFT as implemented in Quantum Espresso code.<sup>28</sup> The exchange-correlation relationship was handled using Perdew-Burke-Ernzerhof's (PBE) generalized gradient approximation (GGA).<sup>29</sup> To accurately estimate the interaction between absorber and adsorbent, we utilized Grimme's dispersion adjustment (D2) in all calculations.<sup>30</sup> A vacuum of 20 Å was applied in the direction perpendicular to the plane to avoid interaction between two neighboring layers. For supercell, a kinetic energy cut-off of 70 Ry was adopted, which is sufficient for the convergence of total energy and structural parameters. During structural optimizations, the Brillouin zone (BZ) is

sampled using Monkhorst-Pack k-mesh of  $5 \times 10 \times 1$  grid in the reciprocal space.<sup>31</sup> The energy convergence value between two successive steps was set at  $10^{-4}$  eV, and the process was repeated until the maximum Hellmann-Feynman forces acting on each atom were less than  $0.001$  eV/Å.

### 4.3 Results and Discussion

#### 4.3.1 Pristine 2D o-B<sub>2</sub>N<sub>2</sub>

*Table 4.1: Comparison of the calculated bond lengths and band gap of the 2D o-B<sub>2</sub>N<sub>2</sub> with previous reports.*

System	Bond length (Å)			Band gap (eV)	Reference
	B-B	N-N	B-N		
o-B <sub>2</sub> N <sub>2</sub>	1.69	1.43	1.43	0.66	Present work
	1.70	1.44	1.44	0.64	22
	1.70	1.44	1.44	0.64	23
	1.70	1.43	1.43	0.64	24
	1.70	1.44	1.44	0.67	25

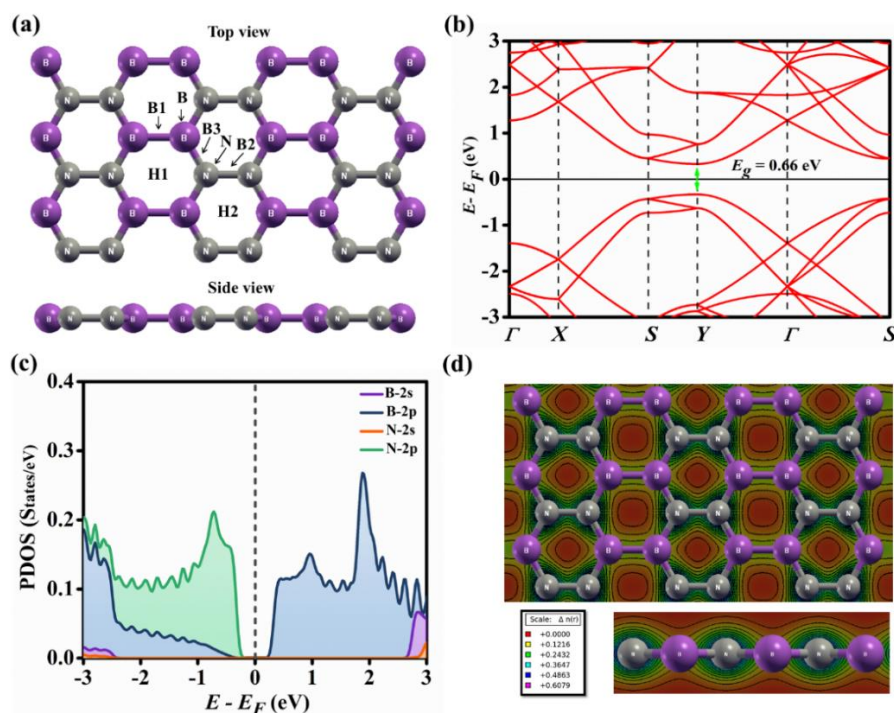


*Figure 4.1: The structural geometry (a), band structure (b), PDOS (c) and charge density contour plot (d) of 2D o-B<sub>2</sub>N<sub>2</sub>.*

To check the potential of 2D o-B<sub>2</sub>N<sub>2</sub> as HER catalyst, we optimized a supercell with dimensions of 3×3×1. Fig. 4.1(a and b) depicts the structural representation and band structure of the 2D o-B<sub>2</sub>N<sub>2</sub>. In order to assess the reliability of our results, we determined the bond lengths and band gap; and compiled the results in Table 4.1. There is a good consistency between the calculated bond lengths and band gap; and the data presented in previous reports.<sup>22-</sup><sup>25</sup> The lattice parameters a and b of the 2D o-B<sub>2</sub>N<sub>2</sub> with a size of 3×3×1 is 13.65 Å and 7.44 Å, respectively. In Fig. 4.1(c), the PDOS of the 2D o-B<sub>2</sub>N<sub>2</sub> shows significant contributions from p orbital of the N atom to the VBM and p orbital of the B atom to the CBM. However, the contribution of s orbitals of B and N atoms near the E<sub>F</sub> is negligible. We analysed Löwdin charges and charge density contour to know the charge spread in the monolayer. The average charges on the B and N atoms are 2.8462e and 5.1346e, respectively. The lower electronegativity of B compared to N explains the lower charge accumulation near the B atoms, which is also evident in the charge density contour plot (Fig. 4.1(d)).

The structural stability of the 2D o-B<sub>2</sub>N<sub>2</sub> is assessed through its formation energy (E<sub>Form</sub>)<sup>32</sup>, which is given by the following expression:

$$E_{\text{Form}} = \frac{E(\text{Monolayer}) - M \times \mu_{\text{B}} - P \times \mu_{\text{N}}}{M + P} \text{ -----(4.1)}$$

In this equation, E(o-B<sub>2</sub>N<sub>2</sub>) is the total energy of the considered system. M and P are the total number of the B and N atoms in the 2D o-B<sub>2</sub>N<sub>2</sub>. The term μ<sub>B</sub> and μ<sub>N</sub> corresponds to the chemical potentials of the B and N atoms. The E<sub>Form</sub> of the 2D o-B<sub>2</sub>N<sub>2</sub> is -0.68 eV determined using equation (4.1). This negative value provides confirmation that the monolayer is stable.

To evaluate the performance of 2D o-B<sub>2</sub>N<sub>2</sub> as a HER catalyst, we conducted H atom adsorption at various sites as depicted in Fig. 4.1(a). Among these sites, the B site exhibited the lowest energy compared to the other cases. For pH=0, the calculated values of ΔE<sub>ads</sub><sup>H</sup> and ΔG<sub>H</sub>

were 1.04 eV and 1.28 eV, respectively (refer to section 3.3.2 of Chapter 3 for formulas and equations). Consequently, bare 2D o-B<sub>2</sub>N<sub>2</sub> is not a desirable HER catalyst due to the positive  $\Delta G_H$  value.

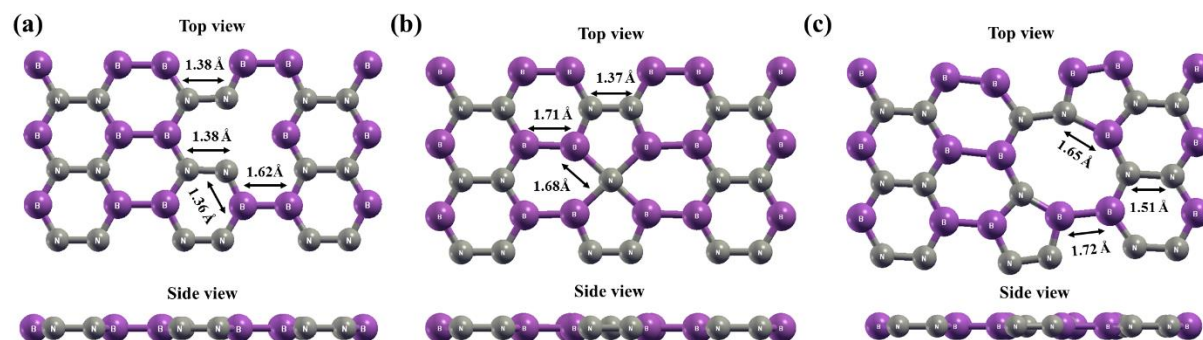


**Figure 4.2: The structural geometry of B (a), N (b) and BN (c) defected 2D o-B<sub>2</sub>N<sub>2</sub>, respectively.**

### 4.3.2 Effect of the Defects on the 2D o-B<sub>2</sub>N<sub>2</sub>

Different techniques for materials design encompass a range of methods, such as dimensional confinement, the introduction of electrical fields or strain, doping of foreign atoms and creation of defects. These techniques can be employed to modify the properties of materials to achieve the desired HER activity. Currently, Ouyang et al. have demonstrated that the introduction of various defects can effectively tune the electronic properties of MoS<sub>2</sub>, leading to a significant enhancement in its HER activity.<sup>33</sup> Inspire from literature survey, in this current investigation, we have introduced vacancy defects into the 2D o-B<sub>2</sub>N<sub>2</sub>. Specifically, we created B, N and BN vacancy defects. Fig. 4.2 represents the structural geometry of the defected 2D o-B<sub>2</sub>N<sub>2</sub>.

The obtained values of  $E_{\text{Form}}$  are -0.51 eV, -0.56 eV and -0.57 eV for B, N and BN defected 2D o-B<sub>2</sub>N<sub>2</sub>, respectively (using equation (4.1)). The negative values signify the exothermic nature and stability of defective monolayers. After introducing a vacancy defects, the bond lengths of B-B, N-N and B-N near the defected region undergo changes (see Fig. 4.2). In case of the B defect, the bond lengths become 1.62 Å (B-B), 1.38 Å (N-N) and 1.36 Å (B-

N), respectively, compared to their original lengths of 1.69 Å, 1.43 Å and 1.43 Å, respectively. For the N defect, the B-B, N-N and B-N bond lengths become 1.72 Å, 1.51 Å and 1.65 Å, respectively. Furthermore, the B-B, N-N and B-N bond lengths in BN defect scenario become 1.72 Å, 1.51 Å and 1.65 Å, respectively. It is important to note that these structural changes resulting from vacancy defects will inevitably impact the electronic properties of the respective monolayers.

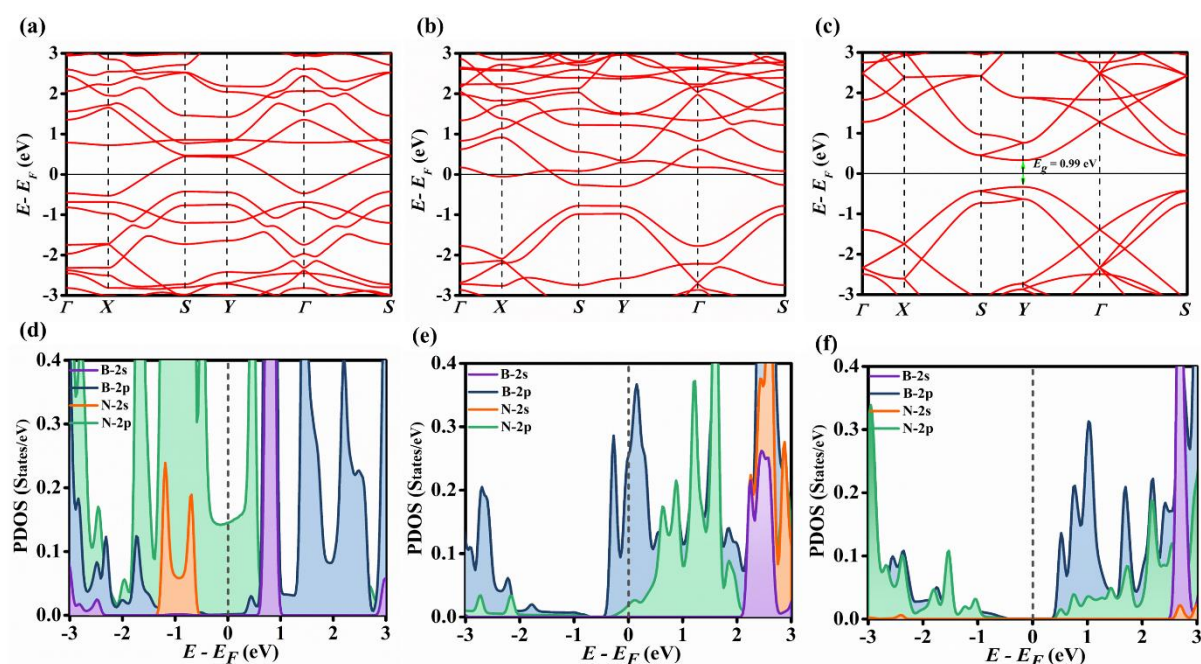


**Figure 4.3: Band structure and PDOS of the B (a and d), N (b and e) and BN (c and f) defected 2D o-B<sub>2</sub>N<sub>2</sub>, respectively.**

After the introduction of defects, the system undergoes a transformation from a semiconductor to a metallic state in the cases of both B and N defects (see Fig. 4.3(a and b)). Introduction of B defect into the 2D o-B<sub>2</sub>N<sub>2</sub> leads to noticeable enhancement in the N-2p orbital at the VBM and at E<sub>F</sub> (see Fig. 4.3(d)). Additionally, compared to the pristine 2D o-B<sub>2</sub>N<sub>2</sub>, there are enhancements in the B-2p orbitals at the CBM. Moreover, the presence of the B vacancy resulted in significant increases in the contributions of the B-2s and N-2s orbitals at the VBM and CBM, respectively which were absent in the pristine case. The N-2p orbitals in the N vacancy defect (as shown in Fig. 4.3(e)) shift to the CBM compared to the case of bare o-B<sub>2</sub>N<sub>2</sub>.

However, the presence of the B-2p, N-2s and B-2s orbitals increases in the CBM due to the defect. In addition, contribution of the various orbitals at  $E_F$  also validates the metallic nature of B and N defected 2D o-B<sub>2</sub>N<sub>2</sub>. In the case of defected BN, certain orbitals, such as N-2p and B-2p, split between VBM and CBM, with a major contribution to the CBM. Moreover, B-2s and N-2s orbitals also significantly contribute to the CBM. The band structure analysis reveals an increased band gap (0.99 eV) in the case of defected BN compared to the pristine case (see Fig. 4.3(c)). This increase is also reflected in the PDOS (see Fig. 4.3(f)). Due to its close proximity to the band gap of typical photocatalyst materials, the BN-defected monolayer shows promise for its use as a photocatalyst.<sup>34,35</sup> To gain insight into the charge distribution after the creation of defects, we have calculated Löwdin charges for each case. The average charges over B (and N) atoms become 2.9954e (and 5.2700e), 2.9820e (and 5.2238e), and 2.8481e (and 5.1325e), respectively in B, N and BN defected 2D o-B<sub>2</sub>N<sub>2</sub>. The creation of vacancy defects alters the Löwdin charge distribution for each case.

### 4.3.3 HER Activity of the Defected 2D o-B<sub>2</sub>N<sub>2</sub>

In order to investigate the HER activity of defected monolayers, we introduced H atom at different sites. We selected the configuration with the lowest energy as the basis for subsequent calculations. The structural representations of H adsorption on B, N and BN defected 2D o-B<sub>2</sub>N<sub>2</sub> are illustrated in Fig. 4.4. The changes in the structural parameters are presented Fig. 4.4. Following the interaction, the H atom is situated at distance of 1.00 Å, 1.19 Å and 1.18 Å from the B, N and BN defected monolayers, respectively. The calculated  $\Delta E_{\text{ads}}^{\text{H}}$  ( $\Delta G_{\text{H}}$ ) values are -1.53 eV (-1.29 eV), -2.27 eV (-2.03 eV) and 0.05 eV (+0.29 eV) for B, N and BN defected 2D o-B<sub>2</sub>N<sub>2</sub>, respectively. The notably negative  $\Delta E_{\text{ads}}^{\text{H}}$  values within the context of B and N defected 2D o-B<sub>2</sub>N<sub>2</sub> signify a strong interaction between them, pointing to their unsuitability as efficient catalysts for the HER activity due to challenges in the desorption stage.

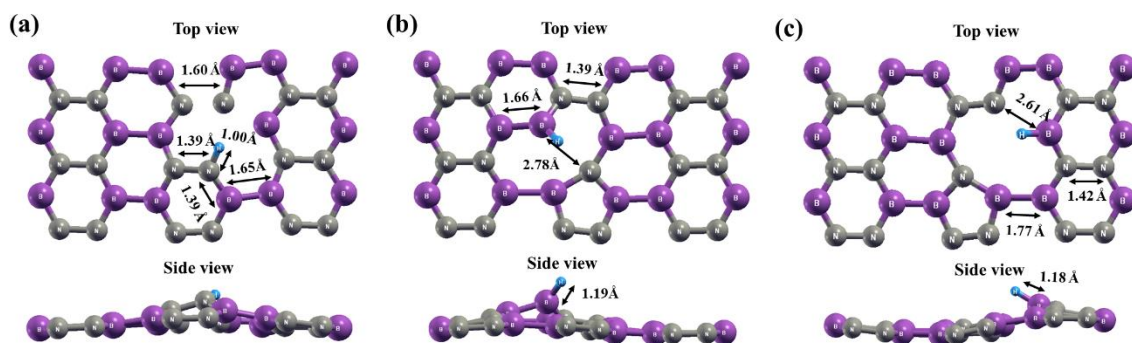


**Figure 4.4:** The structural geometry of the H adsorbed over B defected (a), N defected (b) and BN defected (c) 2D  $o\text{-B}_2\text{N}_2$ , respectively.

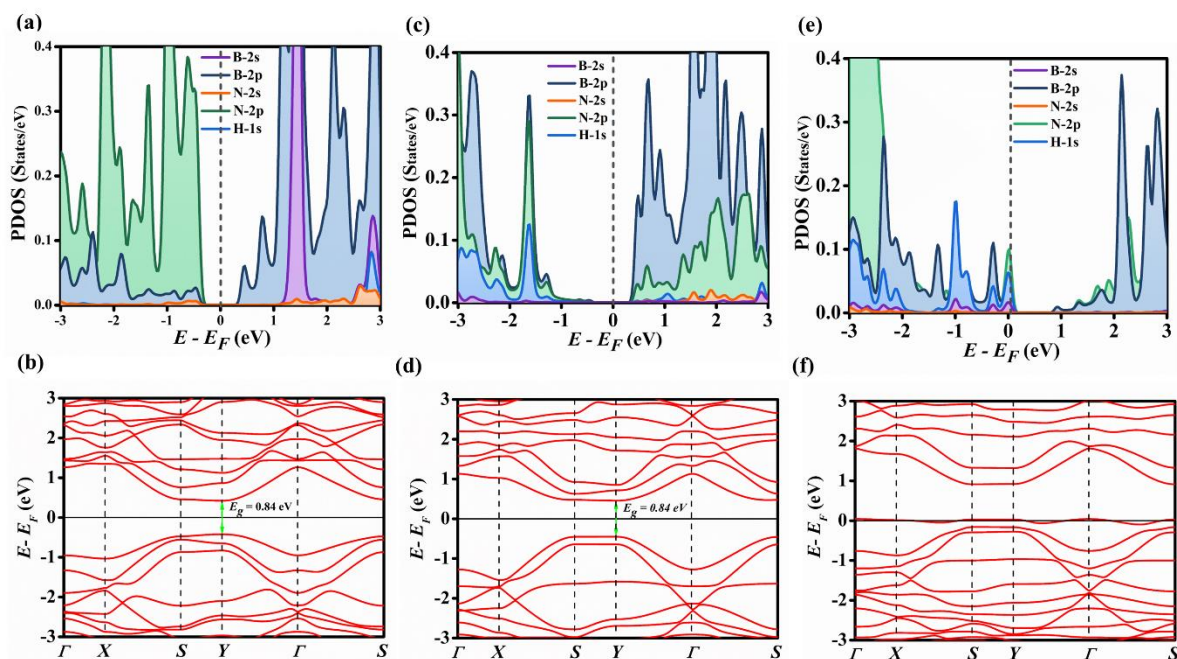


**Figure 4.5:** PDOS and band structure of the H adsorbed over B defected (a and b), N defected (c and d) and BN defected (e and f) 2D  $o\text{-B}_2\text{N}_2$ , respectively.

In the situation where a monolayer contains B defect, the presence of adsorbed H induces changes in its structure. These changes are notable through the modifications in bond distances. Specifically, the bond lengths differ significantly: 1.65 Å for B-B, 1.39 Å for N-N, and 1.39 Å for B-N bonds, in comparison to the scenario without adsorption. These alterations arise due to the strong interaction between H and the monolayer. One of the N-N bonds adjacent to the adsorption site experiences elongation from 1.38 Å to 1.60 Å, resulting in the rupture of the bond between these atoms. The earlier discussion emphasizes the distortion in the structure caused by the interaction of the H to the monolayer. This phenomenon is readily observable in

the geometric arrangement of the structure as depicted in Fig. 4.4(a). The alteration in the structure exerts a discernible impact on the electronic properties, resulting in a significant decrease in the PDOS at the  $E_F$ , as evidenced in Fig. 4.5(a), when contrasted with the B defected monolayer (refer to Fig. 4.3(d)). With the introduction of H through adsorption, the N-2p orbital undergoes a shift towards the VBM, accompanied by a corresponding shift of the N-2s orbitals towards the CBM. However, the presence of B-2s and B-2p orbitals remains relatively unchanged, owing to H's propensity to adsorb onto the N atom within the B defected monolayer, as depicted in Fig. 4.4(a). Moreover, the H-1s orbital undergoes a division into VBM and CBM, thereby affirming the robust interaction between the H atom and B defected monolayer. Following the adsorption of H, the system undergoes a transformation into a semiconducting state, characterized by the band gap of 0.84 eV. This shift is distinctly evident in both band structures, depicted in Fig. 4.5 (b), and the PDOS, as illustrated in Fig. 4.5(a). The observation from Löwdin charge transfer reveals a charge loss of 0.1953e from H to the B defected 2D o-B<sub>2</sub>N<sub>2</sub>.

The H adsorption on the monolayer with N defect results in a similar structural distortion to what is observed when H is adsorbed on the monolayer with B defect. This resemblance becomes evident due to the elongation of bond lengths: 1.66 Å for B-B, 1.39 Å for N-N and 2.78 Å for B-N, in comparison to the scenario without H adsorption. This elongation of bonds is attributed to the strong interaction between the adsorbed H and N defected 2D o-B<sub>2</sub>N<sub>2</sub>. Specifically, the bond length between B and N atoms near the adsorption site stretches from 1.68 Å to 2.78 Å, leading to the breaking of the bond between these atoms (see Fig. 4.4(b)). The impact of H adsorption on the structure becomes visually evident in the changed structural parameters, as depicted in Fig. 4.4(b). As previously discussed, alterations in electronic properties result in a sudden PDOS decrease at the  $E_F$ , contrasting with the monolayer N defect scenario (see Fig. 4.3(c)), indicating electronic configuration shifts (Fig.

4.5(c)). Specifically, the presence of the B-2p orbital becomes more pronounced in both VBM and CBM. In contrast, the contribution of the N-2p orbital increases in the VBM but reduces in the CBM due to interactions between H and B atoms, causing the breaking of B-N bonds (see Fig. 4.4(b)). Moreover, the involvement of B-2s and N-2s orbitals in the CBM decreases compared to the case without adsorption. The influence of H is evident in the splitting of the H-1s orbital, affecting the CBM significantly and confirming a strong interaction with N defected 2D o-B<sub>2</sub>N<sub>2</sub>. This interaction results in a transition of the system's electronic behaviour from metallic to semiconducting, with the band gap of 0.84 eV. This change is clearly observed in the band structure depiction (see Fig. 4.5(d)) and the PDOS (see Fig.5(c)). The semiconducting property emerges due to the absence of B-2p and N-2p orbitals at the Fermi level after the adsorption of H. A detailed analysis of the electronic Löwdin charge distribution reveals that approximately 0.0204e elementary charges are transferred from the H atom to N defected 2D o-B<sub>2</sub>N<sub>2</sub>, indicating a charge redistribution due to the interaction.

Regarding the BN defected 2D o-B<sub>2</sub>N<sub>2</sub>, the obtained values of  $\Delta E_{\text{ads}}^{\text{H}}$  (and  $\Delta G_{\text{H}}$ ) at pH = 0 are 0.05 and 0.29 eV, respectively. The comparison of optimal  $\Delta G_{\text{H}}$  values between the pristine and the defected 2D o-B<sub>2</sub>N<sub>2</sub> underscores the favourable attributes of the BN defected 2D o-B<sub>2</sub>N<sub>2</sub> as a promising photocatalyst for facilitating HER activity at pH = 0. The H adsorption onto the BN defected 2D o-B<sub>2</sub>N<sub>2</sub> leads to a similar structural distortion as observed with H adsorption on B and N defected 2D o-B<sub>2</sub>N<sub>2</sub>. This is clearly indicated by the increased bond lengths: 1.77 Å for B-B, 1.42 Å for N-N and 2.61 Å for B-N, compared to the without adsorption case. These bond length increments result from the interaction between monolayer and the H atom. Specifically, the B-N bond close to the adsorbed H atom extends from 1.65 Å to 2.61 Å, causing a substantial elongation of the bond and eventual breaking between them, as portrayed in Fig. 4.4(c). The aforementioned discussion highlights the structural distortion caused by H adsorption and this distortion is further visually evident in the structural

arrangement illustrated in Fig. 4.4(c). These structural adjustments are also reflected in the electronic characteristics of the system, resulting in a notable augmentation of the PDOS at  $E_F$ , as showcased in Fig. 4.5(e). This stands in stark contrast to the configuration without adsorption, as depicted in Fig. 4.3(f). Upon the introduction of H adsorption, there is an amplification in the contribution originating from B-2p, B-2s, N-2p and N-2s orbitals within the VBM. This is concurrently accompanied by a reduction within the CBM, diverging from the scenario where no adsorption occurs. This shift implies a reinforced interaction between the H atom and the BN defected monolayer. This interaction is corroborated by the presence of the H-1s orbital within the CBM. The H adsorption causes a transition of band gap from a semiconducting state to a metallic state. This alteration is vividly portrayed in the band structure diagram in Fig. 4.5(f), as well as the PDOS plot in Fig. 4.5(e). The primary reason for this metallic conductance is mainly due to the close alignment of the N-2p, B-2s and H-1s orbitals with the  $E_F$  following the adsorption process. From the Löwdin charge transfer, we observe a charge loss of  $0.0257e$  from the H atom to the BN defected 2D o-B<sub>2</sub>N<sub>2</sub>.

Fig. 4.6(a) illustrates the difference in charge density (CDD) involving the H adsorbed BN defected 2D o-B<sub>2</sub>N<sub>2</sub>, the BN defected 2D o-B<sub>2</sub>N<sub>2</sub> and the isolated H atom. The yellow and blue shaded areas represent regions of charge deficiency and accumulation, respectively. As shown in Fig. 4.6(a), it is apparent that the yellow region, denoting an area of charge deficiency, is positioned directly above the H atom. This observation is in line with the outcomes of the Löwdin charge transfer, which also suggests a charge transfer from the H atom.

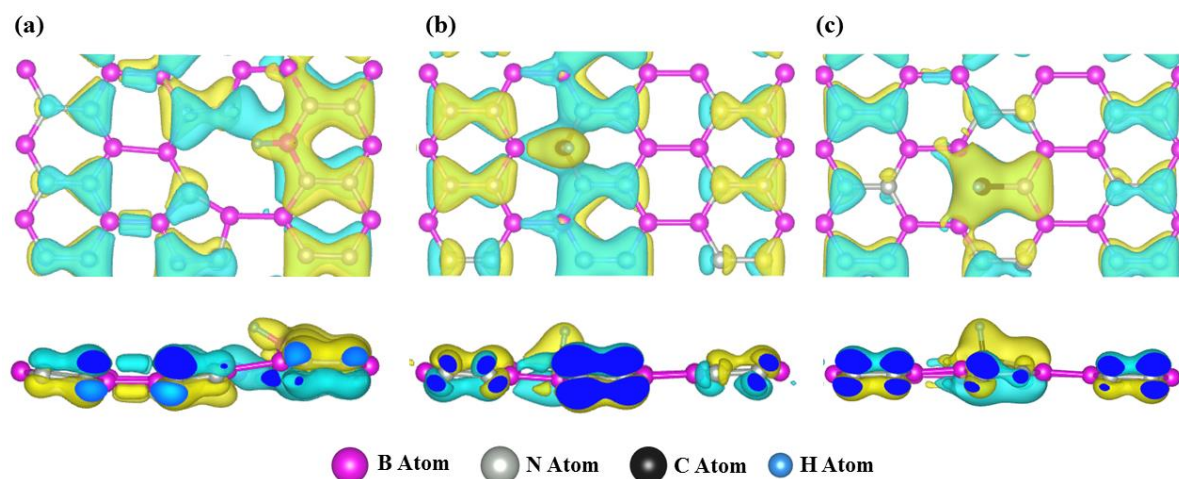


**Figure 4.6:** A charge density difference illustrations of the H adsorbed over BN defected (a), C doped at B site (b) and C doped at N site (c) of the 2D o-B<sub>2</sub>N<sub>2</sub>, respectively.

#### 4.3.4 Effect of the Carbon Doping on the 2D o-B<sub>2</sub>N<sub>2</sub>

The doping of foreign atom offers an excellent approach to tailor the properties of various monolayers according to specific requirements. Notably, Wan et al. achieved property modification in p-BN through the C doping, rendering it suitable as a metal-free photocatalyst for overall water splitting under visible light exposure.<sup>21</sup> In the current investigation, we introduced C atoms into both the B and N sites of the 2D o-B<sub>2</sub>N<sub>2</sub> to modulate its HER activity. Fig. 4.7 illustrates the structural geometries of the 2D o-B<sub>2</sub>N<sub>2</sub> with C doping at the B and N sites. Initially, we computed the  $E_{\text{Form}}$  of the C doped configurations at the B and N sites of the 2D o-B<sub>2</sub>N<sub>2</sub> using the following equation:

$$E_{\text{Form}} = \frac{E(\text{C doped 2D o-B}_2\text{N}_2) - M \times \mu_{\text{B}} - P \times \mu_{\text{N}} - Z \times \mu_{\text{C}}}{M+P+Z} \text{ ----(4.2)}$$

where  $E(\text{C doped 2D o-B}_2\text{N}_2)$  represents the total energy of the C doped 2D o-B<sub>2</sub>N<sub>2</sub>. M, P and Z denotes total number of the B, N and C atoms in the system. The  $\mu_{\text{C}}$  represents the chemical C atom. Using equation (4.2), the obtained  $E_{\text{Form}}$  values are -0.62 eV and -0.64 eV for C doping at the B and N sites of the 2D o-B<sub>2</sub>N<sub>2</sub>, respectively. These negative values confirm the stable nature of the C doped 2D o-B<sub>2</sub>N<sub>2</sub>.

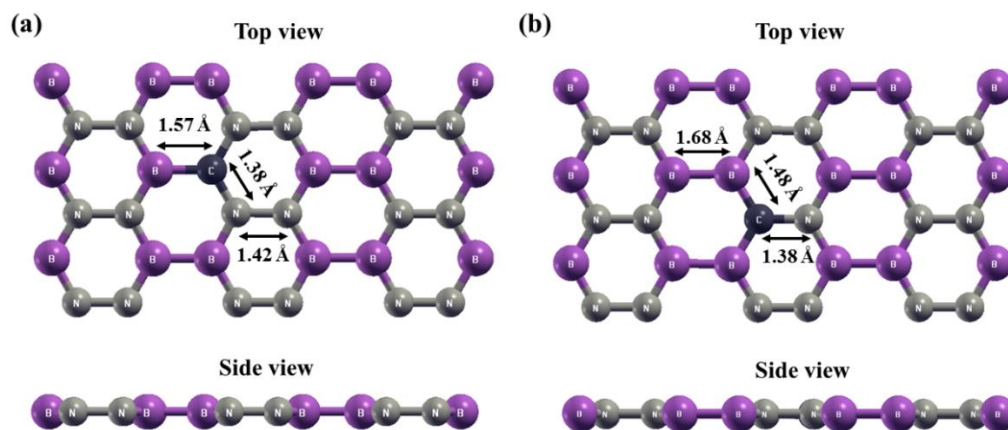


Figure 4.7: The structural geometry of C doped at B site (a) and at N site (b) of 2D o-B<sub>2</sub>N<sub>2</sub>.

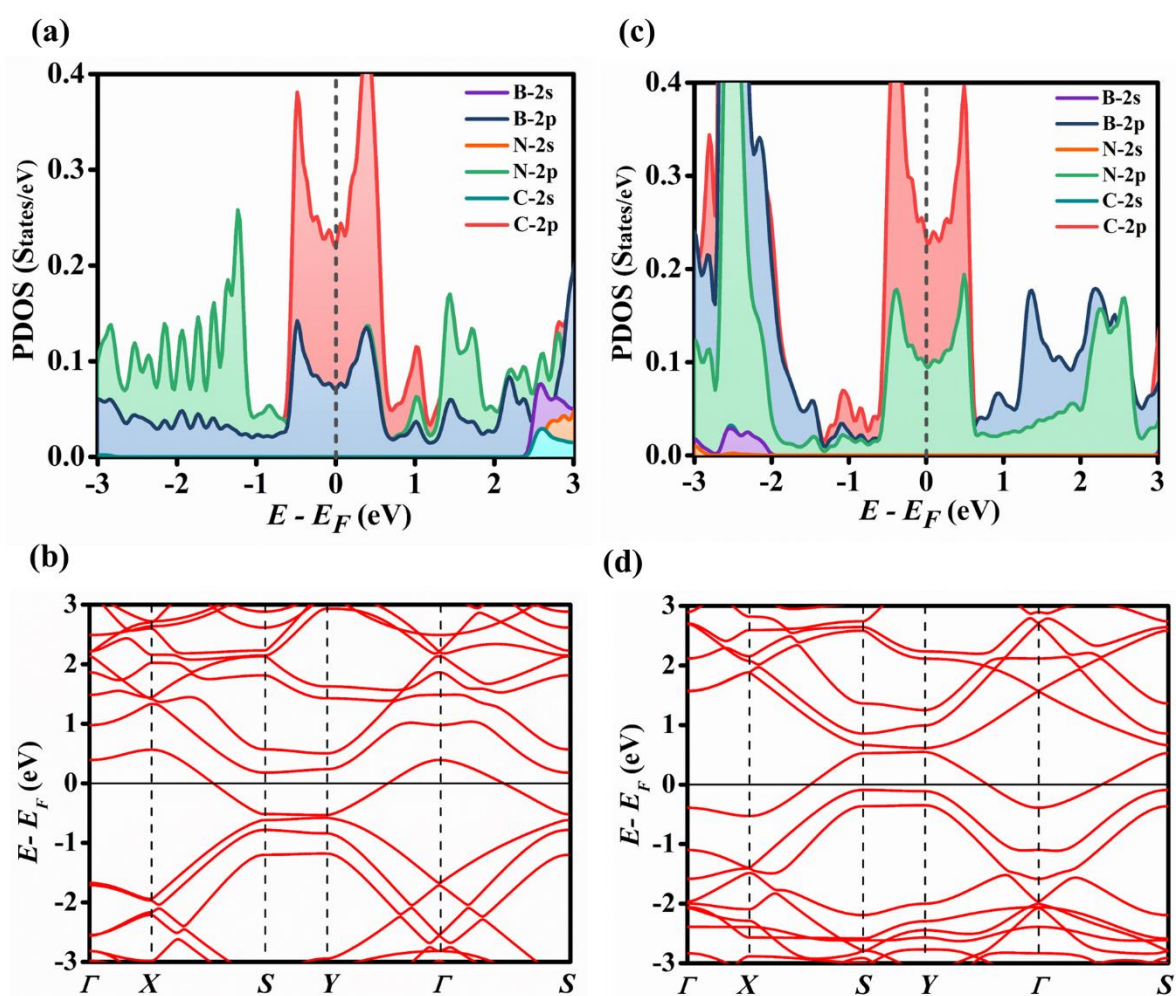


Figure 4.8: PDOS and band structure of the C doped at B site (a and b) and at N site (c and d) of 2D o-B<sub>2</sub>N<sub>2</sub>, respectively.

When C atom is introduced as a dopant at the B site (as depicted in Fig. 4.7(a)), specific bond lengths are observed: B-C is 1.57 Å, C-N is 1.38 Å and N-N is 1.42 Å. This C doping induces significant modulation in the electronic characteristics of 2D o-B<sub>2</sub>N<sub>2</sub>. This change

becomes evident from the band structure and PDOS plots illustrated in Fig. 4.8. In the case of C doping at the B site (depicted in Fig. 4.8(a)), the VBM and CBM reveal nearly equal splitting among B-2p, C-2p and N-2p orbitals. However, the CBM experiences a reduction/increment in B-2p/N-2p orbital contributions compared to bare 2D o-B<sub>2</sub>N<sub>2</sub>. Additionally, the C-2s, B-2s and N-2s orbitals scarcely impact the CBM, mirroring the behaviour of bare 2D o-B<sub>2</sub>N<sub>2</sub>. The band structure (depicted in Fig. 4.8(b)) indicates a transition from semiconductor behaviour to metallic behaviour upon introducing the C atom at B site. This shift towards metallic behaviour can mainly be attributed to the participation of C-2p, B-2p and N-2p orbitals at the E<sub>F</sub>, as illustrated in Fig. 4.8(a).

In the scenario when the C is introduced at the N site (refer to Fig. 4.7(b)), the bond lengths of B-B, B-C and C-N are measured to be 1.68 Å, 1.48 Å and 1.38 Å respectively. When C occupies the N site (as depicted in Fig. 4.8(c)), the B-2p, C-2p and N-2p orbitals show nearly equal division within the VBM and CBM, resembling the behaviour observed for C doped at B site of 2D o-B<sub>2</sub>N<sub>2</sub>. However, the presence of B-2p/N-2p orbitals increases/decreases within the VBM and CBM respectively, unlike the situation with C doping at the B site. Additionally, the contribution of C-2s, B-2s and N-2s orbitals to the VBM is minimal, in direct contrast to the behaviour seen with C doped at the B site in the monolayer. The analysis of the band structure (as seen in Fig. 4.8(d)) also unveils a metallic characteristic in the system following the introduction of the C atom at N site. This metallic characteristic is attributed to the involvement of C-2p, B-2p and N-2p orbitals at E<sub>F</sub>, similar to the behaviour observed when C is doped at the B site within the monolayer (as illustrated in Fig. 8(c)). From the PDOS analysis (refer to Fig. 4.8(a and c)), a clear overlap between the C-2p and B-2p orbitals at E<sub>F</sub> indicates a strong interaction and hybridization between these orbitals. Upon introducing C doping, the system exhibits metallic behaviour, resulting in an increase in its electronic conductivity.

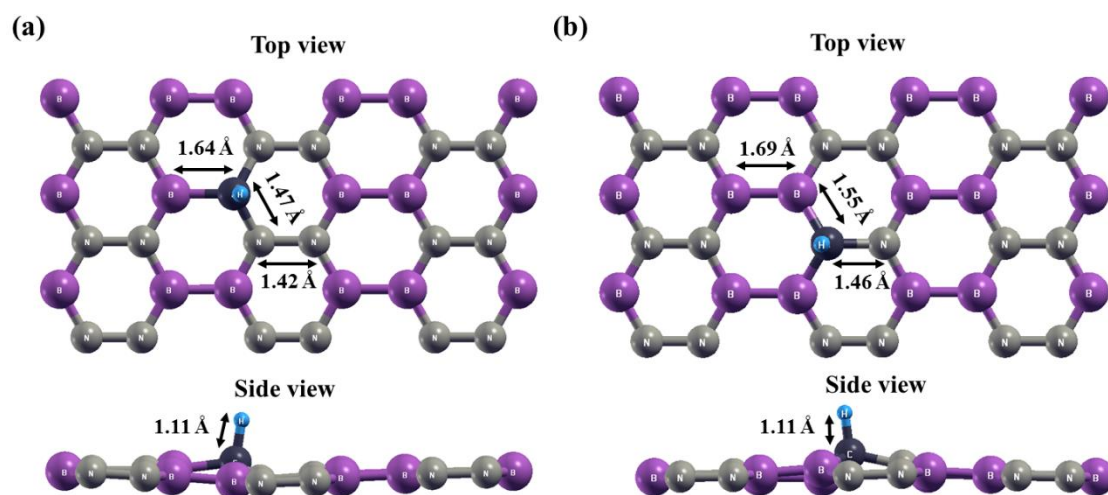
4.3.5 HER Activity of the Carbon doped 2D o-B<sub>2</sub>N<sub>2</sub>

Figure 4.9: The structural geometry of the H adsorbed over C doped at B site (a) and at N site (b) of 2D o-B<sub>2</sub>N<sub>2</sub>, respectively.

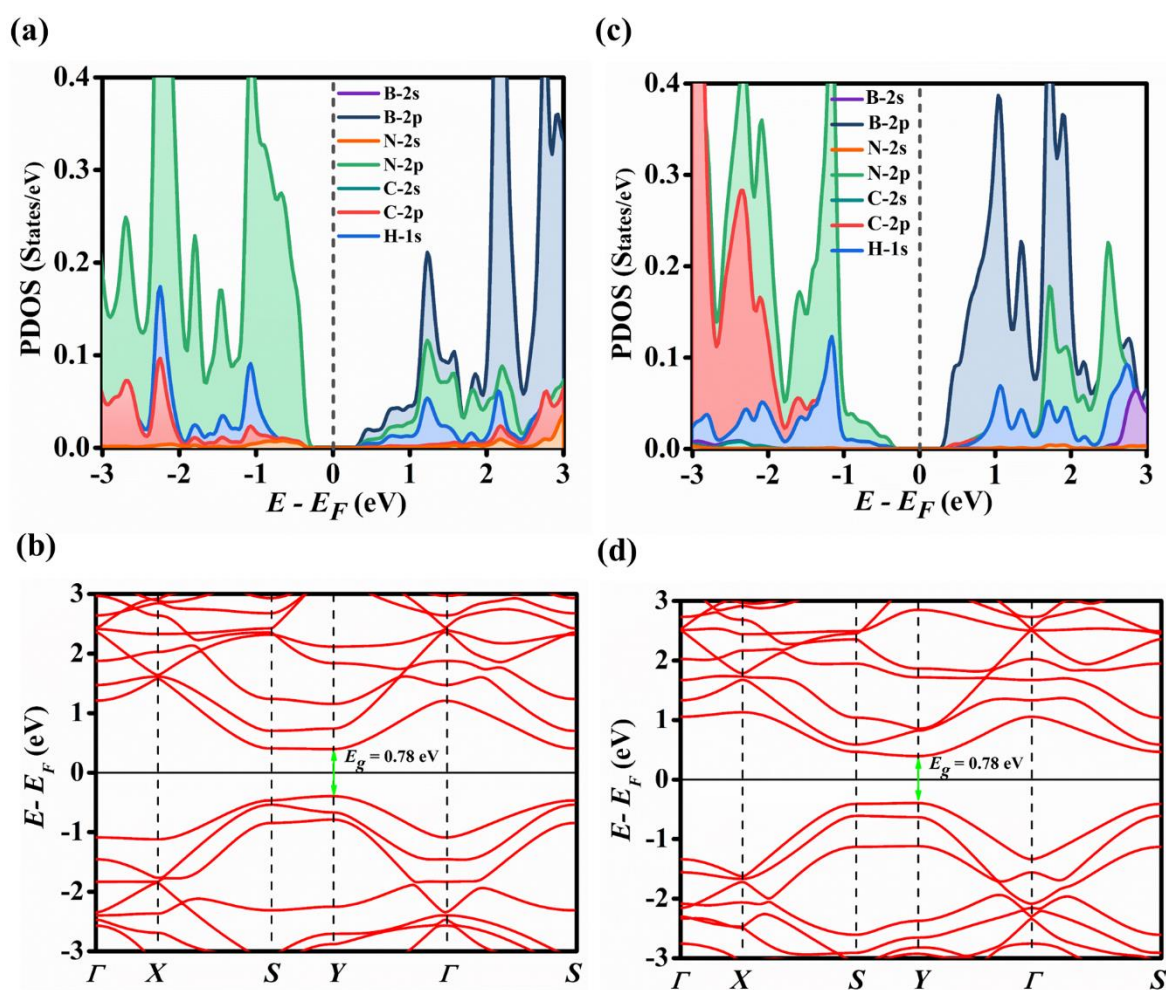


Figure 4.10: PDOS and band structure of the H adsorbed over C doped at B site (a and b) and at N site (c and d) of 2D o-B<sub>2</sub>N<sub>2</sub>, respectively.

To check the HER activity of the C doped 2D o-B<sub>2</sub>N<sub>2</sub>, we carried out simulations involving the adsorption of the H atom at various locations on both types of monolayers. Among the investigated sites, it was observed that the C site had the lowest energy in both cases of C doped configurations. The optimized arrangements of H adsorption on C doped configurations at the B site and N site of the 2D o-B<sub>2</sub>N<sub>2</sub> are presented in the Fig. 4.9(a and b), respectively. Changes in the structural parameters are visually represented in the Fig. 4.9. Initially, the H atom was situated at a distance of 2 Å from the respective sites. After the optimization process, the distance of H atom from the C atom in both monolayers was refined to 1.11 Å. The computed  $\Delta E_{\text{ads}}^{\text{H}}$  values for C doping at the B and N sites within the monolayer are -0.41 eV and -0.45 eV correspondingly. Regarding the adsorption of H for C doped cases, the calculated  $\Delta E_{\text{ads}}^{\text{H}}$  values indicate an optimal level of interaction. This balance strikes a point where the interaction is neither excessively strong nor overly weak when compared to the defective and pristine scenarios. This optimal interaction signifies a favourable indication for the catalytic activity of the HER. Additionally, the calculated  $\Delta G_{\text{H}}$  values (at pH = 0) have been evaluated as -0.17 eV and -0.21 eV for the respective cases. Hence, the obtained  $\Delta G_{\text{H}}$  value for C doped 2D o-B<sub>2</sub>N<sub>2</sub> is comparable to that of the best HER catalyst, namely Pt metal.

Following the adsorption of H onto a monolayer doped with C at the B site, changes in bond lengths are evident. Specifically, the distance of the B-C bond extends from 1.57 Å to 1.64 Å, while the C-N bond distance shifts from 1.38 Å to 1.47 Å. Importantly, the N-N bond distance remains unchanged (see Fig. 4.9(a)). Fig. 4.9(a) also reveals a slight shift of the C atom toward the H atom after H adsorption, resulting in minimal structural modifications. An investigation of PDOS in Fig. 4.10(a) illustrates the noticeable splitting of N-2p, B-2p and C-2p states in both the VBM and CBM. Notably, N-2p and B-2p states strongly influence the VBM and CBM, respectively. The H-1s state equally contributes to both the VBM and CBM, confirming its interaction with the monolayer. Following the adsorption of H, the system

transitions into a semiconductor state with a calculated the band gap of 0.78 eV (depicted in Fig. 4.10(b)). This change is attributed to the absence of contributions from N-2p, B-2p and C-2p states from the  $E_F$ . This is in contrast to the scenario of C doping at the B site of the monolayer. In the Löwdin charge transfer analysis, a charge of 0.1424e is observed to be transferred from the H atom to the monolayer. Additionally, the charge deficiency region over H atoms is also evident from the CDD plot (refer to Fig. 4.6(b)). This observation further substantiates the charge transfer analysis.

In the context of H adsorption onto the C doped at N site of the monolayer, changes are observed in the bond lengths of B-B, B-C and C-N. However, after H adsorption, they have shifted to 1.69 Å, 1.55 Å and 1.46 Å from 1.68 Å, 1.48 Å and 1.38 Å, respectively. This alteration is also visually represented in Fig. 4.9(b), which highlights that the C atom moves slightly closer to the H atom upon adsorption. Similar structural modifications are also observed when H is adsorbed over C doped at the B site of the monolayer. In the analysis of the PDOS depicted in the Fig. 10(c), changes around the VBM and CBM are noticed. The splitting of N-2p and B-2p orbitals is prominent in the VBM and CBM regions respectively. Notably, the contribution of N-2p/B-2p orbitals to VBM/CBM outweighs the scenario where C is doped at the N site of the monolayer. Moreover, the C-2p orbital shifts towards the VBM. However, the collective impact of C-2s and N-2s/B-2s orbitals remains minor in the CBM and VBM respectively. The H-1s orbital is distributed between VBM and CBM, confirming its interaction with the monolayer, similar to the case of H adsorption over C doped at the B site. Upon H adsorption, a transition from a metallic state to a semiconducting state occurs, characterized by the band gap of 0.78 eV, as shown in Fig. 4.10(d). This shift results from the reduction in contributions from N-2p, B-2p and C-2p near the  $E_F$ , unlike the situation with C doping at the N site. A comparable trend is observed in the case of H adsorption over C doped at the B site. In Löwdin charge transfer analysis, 0.1706e charge is transferred from H to the

monolayer. The CDD plot (Fig. 4.6(c)) confirms charge deficiency over H atom, supporting the analysis.

### 4.3.6 Effect of pH on the HER activity

For pH values ranging from 1 to 7 in an acidic medium, the calculated  $\Delta G_H$  ranges from -0.17 eV to 0.24 eV for C doping at the B site and from -0.21 eV to 0.20 eV for C doping at the N site as presented in Table 4.2. These values progressively approach zero when compared to the defective and pristine 2D o-B<sub>2</sub>N<sub>2</sub> across the specified pH range. The calculated  $\Delta G_H$  values suggest that the C doped 2D o-B<sub>2</sub>N<sub>2</sub> is highly effective for HER activity over this mentioned pH range. In the case of the BN defected 2D o-B<sub>2</sub>N<sub>2</sub>,  $\Delta G_H$  is close to zero only at pH=0, which indicates its suitability as HER catalyst at pH=0.

**Table 4.2: Calculated Gibbs free energy (at pH = 0 to 7) of pristine, defected and C doped 2D o-B<sub>2</sub>N<sub>2</sub> for HER activity.**

pH	$\Delta G_H$ (eV)					
	Pristine	defected			C doped	
		B	N	BN	at B site	at N site
0	1.28	-1.29	-2.03	0.29	-0.17	-0.21
1	1.33	-1.23	-1.97	0.34	-0.11	-0.15
2	1.39	-1.17	-1.91	0.40	-0.05	-0.09
3	1.45	-1.11	-1.85	0.46	0.00	-0.03
4	1.51	-1.05	-1.79	0.52	0.06	0.02
5	1.57	-0.99	-1.73	0.58	0.12	0.08
6	1.63	-0.93	-1.67	0.64	0.18	0.14
7	1.69	-0.87	-1.61	0.70	0.24	0.20

### 4.3.7 Stability of the HER Catalysts from AIMD Simulations

Based on the preceding discussion, it is evident that both the introduction of the C dopant and presence of the BN defect contribute to improved HER activity of the 2D o-B<sub>2</sub>N<sub>2</sub>. Therefore, the thermal stability analysis of the BN defected and C doped 2D o-B<sub>2</sub>N<sub>2</sub> is

conducted through AIMD simulations at a temperature of 300 K, employing the NVT ensemble as implemented in the VASP code. The comparison between the structural geometries observed at 0 K and 300 K is illustrated in Figure 4.11. It is noteworthy that the extent of structural distortion exhibited at 300 K is exceedingly minimal. This observation strongly suggests a high level of thermodynamic stability within the system.

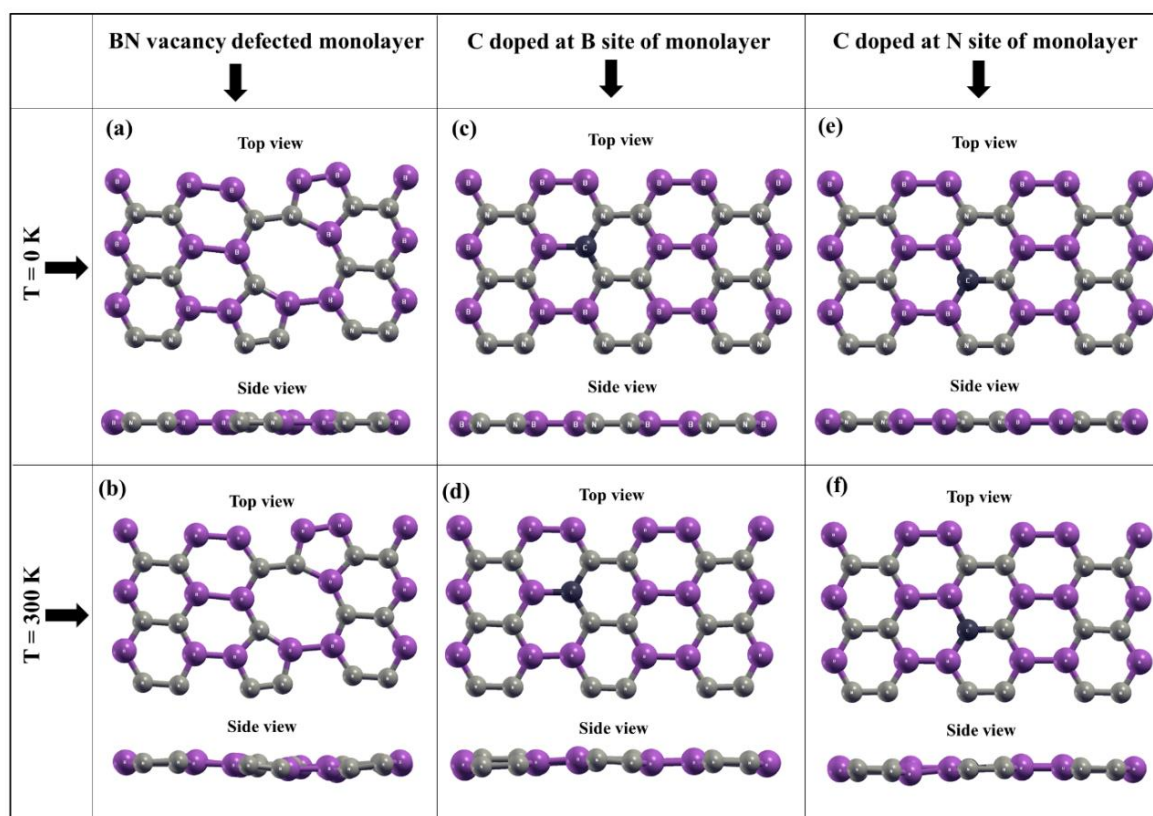


**Figure 4.11:** The comparison of the structure plots at 0 K and 300 K of BN defected (a and b), C doped at B (c and d) and N sites (e and f) of the 2D  $\alpha$ - $B_2N_2$ , respectively.

#### 4.3.8 Drawing Comparison with Previous Studies

Based on the preceding discussion, it is evident that the introduction of the C dopant and the presence of BN defect significantly enhance the HER activity of the 2D  $\alpha$ - $B_2N_2$ . This is further corroborated by the data presented in Fig. 4.12, specifically the reaction coordinates plot. It is quite apparent from this plot that the 2D  $\alpha$ - $B_2N_2$  with C doping and BN vacancy defect demonstrates  $\Delta G_H$  value that is notably close to zero, in stark contrast to the pristine and the B and N defected  $\alpha$ - $B_2N_2$  monolayers, respectively.

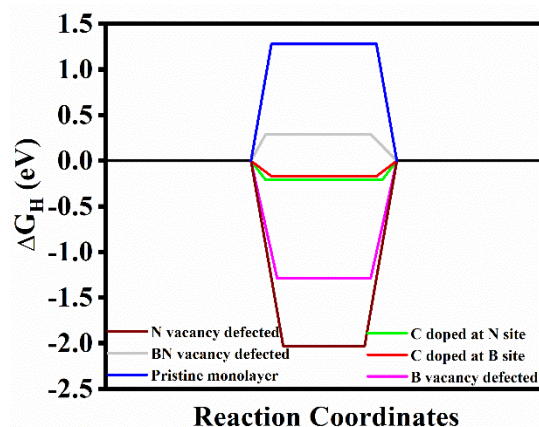


**Figure 4.12:** Reaction coordinates of pristine, defected and C doped 2D o-B<sub>2</sub>N<sub>2</sub> for HER.

The HER activity exhibited by the C doped 2D o-B<sub>2</sub>N<sub>2</sub> outshines several other materials such as C vacancy graphene ( $\Delta G_H = -2.10$  eV)<sup>36</sup>, N doped graphene ( $\Delta G_H = -0.69$  eV)<sup>36</sup>, B doped g-C<sub>3</sub>N<sub>4</sub> ( $\Delta G_H = -0.90$  eV)<sup>37</sup>, P doped g-C<sub>3</sub>N<sub>4</sub> ( $\Delta G_H = -0.37$  eV)<sup>37</sup>, B doped  $\alpha$ -CN ( $\Delta G_H = -0.40$  eV)<sup>32</sup>, Na doped SnSe<sub>2</sub> ( $\Delta G_H = -0.29$  eV)<sup>38</sup>, h-AlC ( $\Delta G_H = -0.502$  eV)<sup>39</sup> and CoOOH ( $\Delta G_H = -0.21$  eV)<sup>40</sup> monolayers. Moreover, the HER activity of the C doped 2D o-B<sub>2</sub>N<sub>2</sub> aligns closely with that of the 2D h-B<sub>2</sub>O ( $\Delta G_H = -0.07$  eV)<sup>41</sup>. Similarly, presence of the BN vacancy within the 2D o-B<sub>2</sub>N<sub>2</sub> ( $\Delta G_H = 0.29$  eV) showcases a commendable level of HER activity. This becomes evident when comparing its performance to that of As doped GeSb ( $\Delta G_H = 0.31$  eV)<sup>42</sup> and haeckelite boron nitride quantum dots ( $\Delta G_H = 0.21$  eV)<sup>43</sup>. Notably, the HER activity of the BN vacancy 2D o-B<sub>2</sub>N<sub>2</sub> surpasses that of Nb doped ZrS<sub>2</sub> ( $\Delta G_H = +0.57$  eV)<sup>44</sup>, Nb doped ZrSSe ( $\Delta G_H = +0.55$  eV)<sup>44</sup> and Nb doped ZrSe<sub>2</sub> ( $\Delta G_H = +0.63$  eV)<sup>44</sup>.

#### 4.4 Conclusions

In brief, an extensive investigation has been carried out using state-of-the-art density functional theory to analyze the HER activity effectiveness of the 2D o-B<sub>2</sub>N<sub>2</sub> in various states: pristine, with defects and under C doping. The intrinsic 2D o-B<sub>2</sub>N<sub>2</sub> displayed not suitability for HER, as indicated by the  $\Delta G_H$ . Introducing vacancy defects induced noteworthy changes in the monolayer's structure and electronic properties. The presence of BN vacancy defect leads to a widening of the band gap from 0.66 eV to 0.99 eV. Remarkably, the BN defected configuration

exhibited  $\Delta G_H$  close to zero compared to B and N defected as well as pristine configurations. This BN defect augmented HER activity by 77.34% in comparison to the pristine configuration at pH = 0. With the inclusion of C doping, the system's behavior transitioned from that of a semiconductor to a metal. The  $\Delta G_H$  of the C doped 2D o-B<sub>2</sub>N<sub>2</sub> approached zero in both scenarios, signifying its suitability for HER. The C doping resulted in 86.71% boost in HER activity at the B site and 83.59% enhancement at the N site relative to the pristine configuration at pH = 0. This improvement was attributed to altered charge distribution following defect creation and C doping. Consequently, our findings propose that the metallic C doped 2D o-B<sub>2</sub>N<sub>2</sub> could effectively act as an "electrocatalysts" within the pH range of 0 to 7. On the other hand, the BN defected 2D o-B<sub>2</sub>N<sub>2</sub>, characterized by a 0.99 eV band gap, displays potential as a "photocatalyst" for HER at pH = 0.

## References

- 1 W. Yang and S. Chen, *Chem. Eng. J.*, 2020, **393**, 124726.
- 2 P. C. K. Vesborg, B. Seger and I. Chorkendorff, *J. Phys. Chem. Lett.*, 2015, **6**, 951–957.
- 3 N. Dubouis and A. Grimaud, *Chem. Sci.*, 2019, **10**, 9165–9181.
- 4 Q. Ma, G. Ren, K. Xu and J. Z. Ou, *Adv. Opt. Mater.*, 2021, **9**, 1–26.
- 5 D. Akinwande et al., *Extrem. Mech. Lett.*, 2017, **13**, 42–77.
- 6 S. Das, M. Kim, J. W. Lee and W. Choi, *Crit. Rev. Solid State Mater. Sci.*, 2014, **39**, 231–252.
- 7 T. Sun, G. Zhang, D. Xu, X. Lian, H. Li, W. Chen and C. Su, *Mater. Today Energy*, 2019, **12**, 215–238.
- 8 D. Wang, X. Bin Li and H. B. Sun, *Nano Lett.*, 2021, **21**, 6298–6303.
- 9 Y. Jiao, Y. Zheng, K. Davey and S.-Z. Qiao, *Nat. Energy*, 2016, **1**, 16130.
- 10 A. Eftekhari, *Int. J. Hydrogen Energy*, 2017, **42**, 11053–11077.
- 11 B. R. Sathe, X. Zou and T. Asefa, *Catal. Sci. Technol.*, 2014, **4**, 2023–2030.
- 12 Y. Tian, Z. Wei, X. Wang, S. Peng, X. Zhang and W. ming Liu, *Int. J. Hydrogen Energy*, 2017, **42**, 4184–4192.
- 13 J. Lim, S. Back, C. Choi and Y. Jung, *ChemCatChem*, 2018, **10**, 4450–4455.
- 14 J. Zhang, S. Hu and Y. Wang, *RSC Adv.*, 2014, **4**, 62912–62919.

- 15 L. L. Feng, Y. Zou, C. Li, S. Gao, L. J. Zhou, Q. Sun, M. Fan, H. Wang, D. Wang, G. D. Li and X. Zou, *Int. J. Hydrogen Energy*, 2014, **39**, 15373–15379.
- 16 Z. F. Huang, J. Song, L. Pan, Z. Wang, X. Zhang, J. J. Zou, W. Mi, X. Zhang and L. Wang, *Nano Energy*, 2015, **12**, 646–656.
- 17 J. Hao, F. Wei, X. Zhang, L. Li, C. Zhang, D. Liang, X. Ma and P. Lu, *Nanoscale Res. Lett.*, 2021, **16**, 130.
- 18 A. I. Siahlo, N. A. Poklonski, A. V. Lebedev, I. V. Lebedeva, A. M. Popov, S. A. Vyrko, A. A. Knizhnik and Y. E. Lozovik, *Phys. Rev. Mater.*, 2018, **2**, 036001.
- 19 D. N. Sredojević, M. R. Belić and Ž. Šljivančanin, *J. Phys. Chem. C*, 2020, **124**, 16860–16867.
- 20 M. Gao, M. Adachi, A. Lyalin and T. Taketsugu, *J. Phys. Chem. C*, 2016, **120**, 15993–16001.
- 21 Q. Wan, F. Wei, Z. Ma, M. Anpo and S. Lin, *Adv. Theory Simulations*, 2019, **2**, 1800174.
- 22 S. Demirci, S. E. Rad, S. Kazak, S. Nezir and S. Jahangirov, *Phys. Rev. B*, 2020, **101**, 1–5.
- 23 R. L. Kumawat and B. Pathak, *Appl. Surf. Sci.*, 2022, **586**, 152850.
- 24 N. Khossossi, W. Luo, Z. Haman, D. Singh, I. Essaoudi, A. Ainane and R. Ahuja, *Nano Energy*, 2022, **96**, 107066.
- 25 R. Rahimi and M. Solimannejad, *Energy and Fuels*, 2021, **35**, 6858–6867.
- 26 M. M. Kadhim, R. Kadhim Mahmood, N. Ali, Z. Sabri Abbas, S. K. Hachim, S. A. H. Abdullaha and A. Mahdi Rheima, *Comput. Theor. Chem.*, 2022, **1218**, 113935.
- 27 M. M. Kadhim, N. Sadoon, S. A. H. Abdullaha, Z. Sabri Abbas, A. Mahdi Rheima and S. K. Hachim, *Inorg. Chem. Commun.*, 2023, **151**, 110461.
- 28 P. Giannozzi et al., *J. Phys. Condens. Matter*, 2009, **21**, 395502.
- 29 J. P. Perdew, K. Burke and Y. Wang, *Phys. Rev. B*, 1996, **54**, 16533–16539.
- 30 S. Grimme, *J. Comput. Chem.*, 2006, **27**, 1787–1799.
- 31 H. J. Monkhorst and J. D. Pack, *Phys. Rev. B*, 1976, **13**, 5188–5192.
- 32 D. Chodvadiya, N. N. Som, P. K. Jha and B. Chakraborty, *Int. J. Hydrogen Energy*, 2021, **46**, 22478–22498.
- 33 Y. Ouyang, C. Ling, Q. Chen, Z. Wang, L. Shi and J. Wang, *Chem. Mater.*, 2016, **28**, 4390–4396.
- 34 B. Özdamar, G. Özbal, M. N. Çınar, K. Sevim, G. Kurt, B. Kaya and H. Sevinçli, *Phys. Rev. B*, 2018, **98**, 045431.
- 35 Y. Zhao, S. Zhang, R. Shi, G. I. N. Waterhouse, J. Tang and T. Zhang, *Mater. Today*, 2020, **34**, 78–91.
- 36 X. Gao, Y. Zhou, Y. Tan, B. Yang, Z. Cheng and Z. Shen, *Int. J. Hydrogen Energy*, 2019, **44**, 14861–14868.

- 37 Y. Zhu, D. Zhang, L. Gong, L. Zhang and Z. Xia, *Front. Mater.*, 2019, **6**, 1–10.
- 38 A. N. Inamdar, N. N. Som, A. Pratap and P. K. Jha, *Int. J. Hydrogen Energy*, 2020, **45**, 18657–18665.
- 39 K. Patel, B. A. Baraiya, N. N. Som, B. Roondhe and P. K. Jha, *Int. J. Hydrogen Energy*, 2020, **45**, 18602–18611.
- 40 S. B. Pillai, B. A. Baraiya, D. Upadhyay, V. Mankad and P. K. Jha, *Int. J. Hydrogen Energy*, 2020, **45**, 23900–23907.
- 41 X. Zhao, X. Yang, D. Singh, P. K. Panda, W. Luo, Y. Li and R. Ahuja, *J. Phys. Chem. C*, 2020, **124**, 7884–7892.
- 42 M. H. Dalsaniya, T. K. Gajaria, N. N. Som and P. K. Jha, *Phys. Chem. Chem. Phys.*, 2020, **22**, 19823–19836.
- 43 R. Jindal, V. Sharma and A. Shukla, *Int. J. Hydrogen Energy*, 2022, **47**, 41783–41794.
- 44 N. N. Som and P. K. Jha, *Int. J. Hydrogen Energy*, 2020, **45**, 23920–23927.